OrbWeaver: A Geometric Optics-Based RIS for Omnidirectional 3D Beam Steering

Xuan Wang[13◇], Liyao Li[2◇], Runchuan Liu[1], Jiameng Bai[1]
Chao Feng[13], Yuhui Ren[1], Xiaojiang Chen[134], Yaxiong Xie[2]
[1]Northwest University, China [2] University at Buffalo, SUNY
[3] Shaanxi Key Laboratory of Passive Internet of Things and Neural Computing
[4]Shaanxi International Joint Research Centre for the Battery-Free Internet of Things

Abstract

Reconfigurable Intelligent Surfaces (RIS) are a key 6G technology for controlling the wireless environment and eliminating signal blockages. However, dominant planar metasurfaces suffer from high cost, complex control, limited 3D coverage, and high beam alignment overhead. This paper presents OrbWeaver, an RIS that replaces complex metasurfaces with a 3D-printed Luneburg lens and a simple reconfigurable RF switching fabric. It leverages geometric optics for cost-effective, programmable signal redirection across an omnidirectional 3D field of view. A key advantage is its ability to perform in-situ power measurements, enabling a decoupled beam alignment protocol that drastically simplifies multi-node coordination. We validate OrbWeaver with mmWave and sub-6 GHz prototypes, demonstrating its frequency-agnostic design. In real-world 5G and Wi-Fi deployments, OrbWeaver eliminates dead zones, achieving throughput gains up to 430 Mbps and 241 Mbps, respectively. Our results establish OrbWeaver as a practical RIS solution to overcome the deployment barriers of conventional metasurfaces.

CCS Concepts

• **Hardware** → **Wireless devices**; • **Networks** → *Programming interfaces*.

Keywords

RIS, Gradient-index lens, In-situ sensing, 3D beam steering

ACM Reference Format:

Xuan Wang[13◇], Liyao Li[2◇], Runchuan Liu[1], Jiameng Bai[1], Chao Feng[13], Yuhui Ren[1], Xiaojiang Chen[134], Yaxiong Xie[2]. 2026. OrbWeaver: A Geometric Optics-Based RIS for Omnidirectional 3D Beam Steering. In *The 32nd Annual International Conference on Mobile Computing and Networking (MobiCom '26), October 26–30, 2026, Austin, TX, USA.* ACM, New York, NY, USA, 17 pages. https://doi.org/10.1145/3795866.3796688

◇ Both authors contributed equally to this research.

MobiCom '26, Austin, TX, USA

ACM ISBN 979-8-4007-2505-0/2026/10
https://doi.org/10.1145/3795866.3796688

1 Introduction

The evolution of wireless communication towards 5G and beyond promises unprecedented connectivity, but the practical realization of this vision is fundamentally constrained by the physics of radio wave propagation [1, 2]. Within modern buildings, signals are routinely obstructed by walls, corners, and other common materials, creating significant coverage gaps or *dead zones*. This challenge is a universal barrier to reliable connectivity, affecting systems across the spectrum from sub-6 GHz Wi-Fi [3] to high-frequency 5G/6G mmWave bands [4, 5]. These physical-layer limitations create complex coverage scenarios that demand a new approach to engineering the wireless environment. As depicted in Figure 1, canonical examples of this problem include redirecting a signal around a corner to serve a user in a non-line-of-sight (NLoS) location and routing a signal from an outdoor base station or an adjacent room through a wall to an indoor user.

To overcome these physical-layer barriers, a new paradigm has emerged: *reconfigurable intelligent surfaces* (RIS) [6, 7]. Rather than merely compensating for the wireless channel, RIS technology offers a transformative approach to intelligently engineer the propagation environment itself, guiding electromagnetic waves around or even penetrating obstacles to eliminate dead zones and establish robust communication links where none previously existed.

The current and dominant approach to realizing RIS technology is through *metamaterial-based planar metasurfaces* [8–10]. These are artificial, two-dimensional surfaces composed of a large, dense array of sub-wavelength, individually programmable resonant elements, often referred to as *meta-atoms*. The operational principle of these surfaces is rooted in fine-grained wavefront manipulation; by applying precise and coordinated phase shifts to each of the hundreds or thousands of constituent meta-atoms via a central controller, the metasurface can collectively shape an impinging electromagnetic wavefront. This fine-grained, per-element control is *incredibly powerful*, enabling *advanced functionalities beyond*

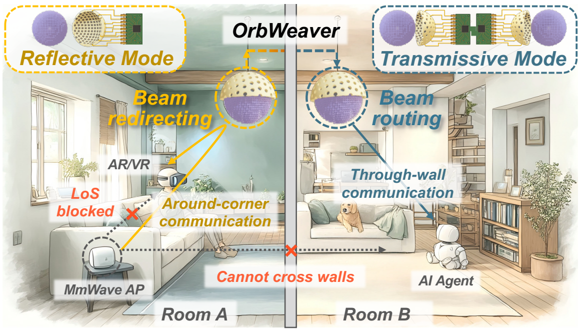

Fig. 1 – Indoor operation modes of OrbWeaver. Reflective mode reflects signals around obstacles (*left*); transmissive mode transmits them through barriers like walls (*right*).

beam steering, such as complex wavefront shaping or even generating frequency shifts [11, 12]. This theoretical power and granular control over the radio environment has made metasurfaces a focal point of academic research.

While powerful, this approach raises a critical question: *for the most common and critical RIS application, i.e., programmable signal steering and penetration, is the complexity and cost of metasurfaces necessary, practical and scalable?* The metamaterial-based approach has fundamental limitations that have largely confined it to laboratory settings and hindered its path to widespread, practical deployment:

- **Hardware and Control Complexity.** Complicated metasurface hardware makes it hard to fabricate, requiring multilayer PCB to integrate and wire a massive number of active RF components, such as PIN diodes or varactors, for each individual meta-atom [13, 14]. This process requires precise layer alignment, the use of specialized materials, component soldering, and complex drilling, driving up costs and manufacturing difficulty. Furthermore, this per-element control mandates *complex and expensive control systems*, often relying on high-cost FPGAs with hundreds of I/O pins to manage the vast number of phase states, a complexity that grows exponentially with the desired phase resolution.
- **Lack of Inherent Sensing.** As *passive signal shapers*, metasurfaces possess no inherent sensing capabilities. They are effectively "blind" and must rely entirely on slow and complex end-to-end feedback from the transmitter (TX) or receiver (RX) to perform beam alignment.
- **Limited 3D Coverage and Inherent Scan Loss.** The planar geometry of metasurfaces inherently limits their three-dimensional coverage. They suffer from significant gain degradation at wide steering angles, a phenomenon known as *scan loss*, where the gain drops as a cosine function of the angle from the broadside direction. This typically restricts their effective field-of-view to only ±60°.

We propose OrbWeaver, a new class of RIS that combines a 3D gradient-index electromagnetic lens [15–17], specifically a *Luneburg lens* [18, 19], with a simple, reconfigurable RF

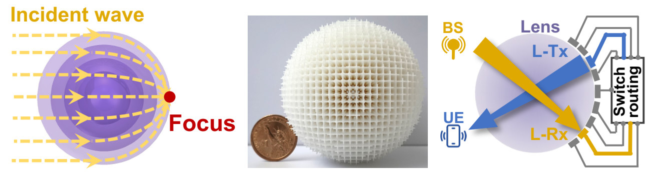

(a) Luneburg lens. (b) 3D-printed lens. (c) Integrated unit.

Fig. 2 – OrbWeaver architecture. The architecture of Luneburg lens and its signal focusing capability (**a**); the 3D-printed realization of lens (**b**); and integrated lens-antenna-fabric OrbWeaver unit working in reflective mode (**c**).

switching fabric, as shown in Figure 2. Our core principle is rooted in its *physics of geometric optics*. A Luneburg lens is a spherical structure that naturally focuses an incoming plane wave from any direction onto a unique focal point on its surface (Figure 2(a)). By the principle of reciprocity, it can also collimate a signal transmitted from a point source on its surface into a highly directional plane wave. We harness this intrinsic property by placing an array of simple antenna elements on the lens's surface. By electronically connecting a pair of these antennas, one designated for reception and the other for transmission, with a low-loss RF switch, we form a single OrbWeaver unit that enables programmable signal redirection or beam rotation (Figure 2(c)). Furthermore, connecting two such units enables a transmissive mode that allows signals to effectively penetrate solid obstacles.

The OrbWeaver architecture offers four key advantages over conventional metasurfaces:

- **Simple Hardware and Control.** The Luneburg lens is 3D-printed at a cost of $6.50 and assembled with commercial off-the-shelf (COTS) RF components, unlike metasurfaces which require complex PCB fabrication. Instead of configuring thousands of phase states, our control system controls a few RF switches to direct the signal.
- **In-Situ Sensing for Autonomous Operation.** Since signals are focused at a specific antenna position, OrbWeaver can measure the focused beam and estimate its *angle-of-arrival* (AoA) without any external feedback or prior knowledge of the transmitter's location. This capability creates a *short feedback loop* that decouples the complex beam alignment problem into simpler, independent searches.
- **Wide 3D Coverage with High Gain.** The Luneburg lens's spherical shape and focusing property inherently provide an omnidirectional field of view. Also, unlike phased arrays that suffer from scan loss, it simply selects a different feed antenna on its surface to change the signal direction, maintaining its high gain regardless of steering angle.
- **Frequency-Agnostic Design.** OrbWeaver's geometric optics principle is *frequency-agnostic*. We can adopt this design to different frequency bands by simply scaling the lens

Table 1: Comparison to existing mmWave works.

Related works	Operating band (GHz)	Tra/Ref	Alignment complexity	Coverage angle	SNR Gain (dB)	TX/RX mobility support
MilliMirror [9]	57–71	R	No Steering	±70°	5-10	×
mmWall [10]	23.5–25.5	T/R	High	±80°	24-30	RX
NR-surface [20]	24	R	High	±70°	15.5-22.5	RX
MoVR [21]	24	R	High	±60°	15-20	RX
mmXtend [22]	26.5–29.5	T	High	±40°	-	RX
OrbWeaver	**26.5-29.5**	**T/R**	Low	**>±80°**	**23-27**	**TX&RX**

and antennas, a principle we validate with our mmWave and sub-6 GHz prototypes (§5.4 and §5.5).

This paper designs, fabricates, and validates the performance of the proposed RIS through a rigorous real-world evaluation. We demonstrate its practical viability by integrating the prototype with commercial 5G mmWave base stations and commodity sub-6 GHz Wi-Fi platforms. The experimental results show significant performance gains; in 5G mmWave deployments, our system achieves throughput improvements of up to 430 Mbps and can restore connectivity to previously unreachable areas. On the Wi-Fi platform, it delivers throughput gains of up to 241 Mbps. These results show the effectiveness of OrbWeaver and demonstrate its readiness as a cost-effective, scalable, and high-performance solution for the NextG wireless environments.

2 RELATED WORK

We compare our system with existing solutions, which can be categorized into antenna and relay systems, metasurfaces/smart surfaces and Luneburg lens applications. Table 1 compares OrbWeaver against state-of-the-art mmWave systems, demonstrating OrbWeaver's superior performance in every category: achieving a broader 3D steering range, higher effective gain, lower beam-alignment complexity, and supporting concurrent transceiver mobility.

Antenna and Relay Systems. To enhance signal power and improve communication quality, a basic solution is to utilize large-scale phased arrays [23–26]. However, these systems require numerous (even hundreds of) high-precision phase shifters and complex feeding networks, resulting in high power consumption and hardware costs. Another approach uses RF repeaters [21, 27, 28], which consist of amplifiers and active components to amplify and forward signals. Although it provides reliable communication, they require protocol modifications, high deployment costs, and suffer from significant power consumption due to their active components. For example, LAVA [27] developed a large relay mesh topology to significantly extend indoor wireless coverage, where each node employed actively controlled amplifiers, consequently increasing the overall system power consumption.

Metasurfaces and Smart Surfaces. Metasurfaces [29–34] are composed of periodically arranged structures that can manipulate electromagnetic waves by controlling the phase and amplitude at each element. By integrating electronic components, these metasurfaces become smart surfaces with programmability capabilities [8, 10, 35–41]. However, these methods face several challenges, including heavy design burdens, fabrication complexity, beam alignment overhead, and limited operation bandwidth.

Luneburg Lens. The Luneburg lens has attracted significant attention for its unique focusing and collimation properties [18, 42–45]. Existing works on Luneburg lens applications can be broadly categorized into three main areas. The first integrates Luneburg lenses with antennas to achieve high-gain beam radiation, transforming spherical waves into directive plane waves for enhanced gain and bandwidth [15–17, 19, 46–49]. The second explores wide-angle beam scanning by deploying multiple feeds around its surface to achieve large field of view coverage [50–54]. The third employs Luneburg lens for retroreflection [55–57], where reflecting planes or reconfigurable metasurfaces at the focal surface support wide-angle reflection and ultra-wideband backscatter. UniScatter [56] utilizes a Luneburg lens to focus incident waves onto a reflector, achieving high-gain retroreflection via reciprocal propagation. However, its passive design lacks active beam routing or steering capability.

In contrast, our system leverages the Luneburg lens in free space not merely for gain, scanning, or reflection, but for arbitrary 3D electromagnetic wave routing. This capability enables adaptive, flexible, and fine-grained control of signal paths, surpassing the inherent structural and functional constraints of conventional Luneburg lens designs.

3 SYSTEM DESIGN

This section presents the design of OrbWeaver, which include three components. A 3D printed gradient index (GRIN) lens (§ 3.1), a hemisphere antenna array positioned around the lens's focal plane (§ 3.2), and a backend control circuit that manages signal routing and processing (§ 3.3). While this design is frequency-agnostic and works for frequencies from sub-6 GHz to mmWave, we will use the mmWave implementation to introduce the system, as it presents more complex design challenges.

3.1 Design of OrbWeaver Lens

In this section, we first introduce the theoretical principles of the Luneburg lens, followed by describing the 3D printing design and fabrication approach that ensures both high-gain performance and cost-effective implementation.

3.1.1 Theory. As described in Appendix §A, Luneburg lens is a spherical gradient-index lens with a radially varying permittivity. In the ideal case, the relative permittivity decreases from 2 at the center to 1 at the surface according to:

$$\varepsilon(r) = 2 - (r/R)^2. \tag{1}$$

This spherical permittivity gradient causes incoming parallel waves (plane waves) to refract continuously and focus onto

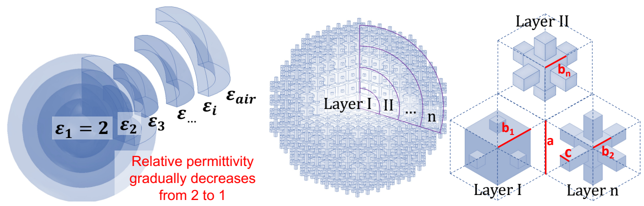

(a) Ideal Luneburg lens model. (b) Practical approximation for 3D printing.

Fig. 3 – Luneburg lens design principle. Ideal model requires a relative permittivity continuously decreases from 2 at the center to 1 at the surface (**a**); This is approximated by 3D printing the lens in discrete layers, where the fill ratio of cubes controls each layer's effective permittivity (**b**).

the opposite side of the sphere. This profile ensures ideal impedance matching with free space at the lens boundary ($\varepsilon(R) = 1$), theoretically eliminating reflection losses at the lens-air interface.

3.1.2 Practical Realization via 3D Printing. Since no natural materials exhibit the continuous permittivity gradient required by Eqn. 1, a practical realization involves approximating this ideal profile. This is commonly achieved by discretizing the lens into *concentric, shell-like layers*, each with a distinct, piecewise-constant effective permittivity, as shown in Figure 3(a). While this could be done by assembling multiple discrete materials, such an approach is costly and complex. A more effective method, and the one used for OrbWeaver, is to leverage 3D printing with a single, low-loss polymer to create a monolithic structure.

This technique relies on geometrically tuning the effective permittivity of each layer. Each layer is structured with sub-wavelength *cubes*, as shown in Figure 3(b). The effective permittivity of each cube is determined by its *filling ratio*: the volumetric proportion of polymer to air. We can finetune the filling ratio by precisely adjusting the cube's internal geometry (a, b, c). This allows the required gradient index profile to be created using only one base material and air.

This design principle is frequency-agnostic and scalable from sub-6 GHz to mmWave bands. As long as the cube is small compared to the wavelength, the lens can be adapted to any target frequency by scaling the physical dimensions of the cubes and the overall lens radius. The final design parameters for a given frequency, such as the number of layers and the specific cube geometries, are selected through a systematic, simulation-driven process. For OrbWeaver, we use electromagnetic simulations to select parameters that achieve high gain and narrow half-power beamwidth (HPBW). Details and final parameters for our 28 GHz and sub-6 GHz prototypes are provided in Appendix §B.

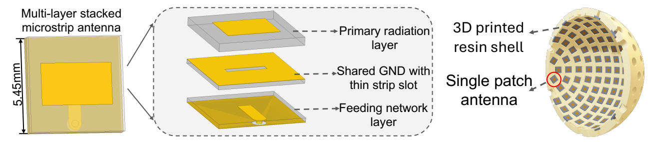

(a) Multi-layer stacked microstrip antenna. (b) 3D printed shell.

Fig. 4 – Hemisphere antenna array architecture and implementation.

3.2 High-Gain Wideband Antenna Array

To exploit the lens's wide-band and spatial focusing capabilities, a high-performance antenna array is required to receive and re-radiate signals from the lens's surface. Designing such an array for the mmWave band presents distinct challenges, as the antennas must offer both high gain and wide operational bandwidth while conforming to the lens's spherical geometry. This section details our design for the antenna elements and the low-cost structure that supports them.

Antenna Design. We select a planar patch (microstrip) antenna architecture for the feed elements due to its compact form factor, ease of fabrication, and compatibility with mmWave circuitry. Our mmWave antenna element is architected as a three-layer stacked microstrip structure: a top layer that serves as the primary radiating patch, a middle layer containing a shared ground plane with a thin coupling slot, and a bottom layer that houses the microstrip feeding network, as shown in Figure 4(a).

Our architecture overcomes the inherent bandwidth limitations of standard microstrip antennas. Specifically, our multi-layer design utilizes electromagnetic slot coupling to broaden the bandwidth. The feeding network on the bottom layer excites the slot, which couples energy to the radiating patch above it. This mechanism excites multiple resonant modes on the patch. By carefully optimizing the geometry of the slot and patch, these modes are designed to overlap, merging to create a single, continuous wideband response. The antenna element itself is realized in a compact footprint of just $5.45mm \times 5.45mm$ and is fabricated using standard printed circuit board (PCB) technology, ensuring it is both inexpensive and scalable.

Supporting Structure. To position the antenna elements correctly on the lens's focal surface, we designed a custom hemispherical supporting shell, shown in Figure 4(b). This shell is fabricated using 3D printing, a method that is both low-cost and ideal for creating the precise, curved geometry required. The shell features precisely located slots that securely hold each antenna element. This integrated design of wide-band antenna elements and a custom-fit, 3D-printed shell provides a practical and cost-effective solution for realizing the complete OrbWeaver system.

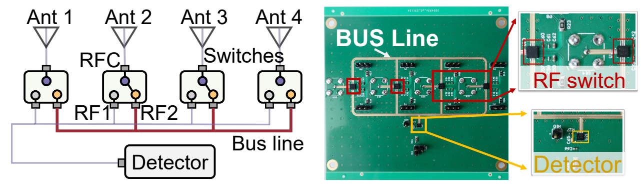

(a) Bus architecture schematic. (b) Fabricated PCB board.

Fig. 5 – Bus-based design fails due to impedance mismatches at mmWave frequencies.

3.3 Reconfigurable RF Switching Fabric for Dynamic Beam Steering

Having established the design of the passive components, the 3D-printed Luneburg lens and the hemispherical antenna array, the final critical element of the OrbWeaver system is the active backend control circuit. This reconfigurable RF routing fabric is what transforms the static hardware into a dynamic and intelligent beam steering platform. This section details the design journey of this fabric, from its core requirements through a flawed initial approach to the novel architecture that enables both robust signal routing and inherent sensing capabilities.

3.3.1 The Challenge: Arbitrary, Low-Loss Antenna Interconnection. The primary requirement for the routing fabric is to dynamically link any antenna in the hemispherical array to any other antenna. In essence, any antenna must be able to serve as a receive element, with its signal routed to any other chosen transmit element on the fly. This fabric must provide such arbitrary antenna-to-antenna connections with high flexibility, wide operational bandwidth, and very low insertion loss to preserve the integrity of the mmWave signal.

The core engineering challenge is not merely switching, but maintaining a stable and predictable RF environment while the connection topology is dynamically reconfigured. In any high-frequency system, maximum power transfer is achieved only when the impedance of the source, transmission path, and load are precisely matched. Any deviation creates reflections that degrade the signal. Consequently, the central design challenge is to achieve impedance-matched, reconfigurable connectivity for *all possible antenna pairings*, a far more stringent requirement than simple static routing.

3.3.2 A Naive Bus Architecture and Its Fundamental Flaws. A straightforward approach to this routing problem is to connect all antennas to a common RF bus, as illustrated in Figure 5. In this design, each antenna is attached to an RF switch, and one throw of every switch is tied to a shared RF line. In principle, connecting a receiving antenna's switch to the bus while simultaneously connecting a transmitting antenna's switch would forward the signal. This bus-style interconnect is conceptually simple and uses minimal hardware, making it initially attractive.

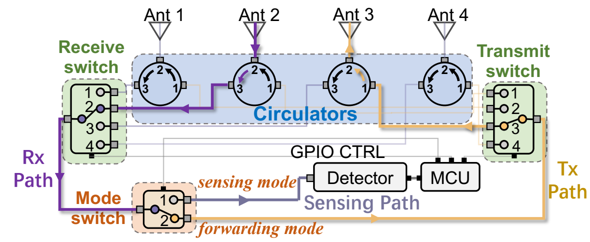

Fig. 6 – Circulator-based architecture.

Despite its simplicity, this design is fundamentally unworkable in the mmWave domain because it disregards the physics of wave propagation. When a pair of antennas is active, the physical transmission lines to all *inactive* antennas remain part of the network as unterminated, "dead-end" branches. The choice of active antennas thus redefines the entire RF path's topology and thus resulting in different composite electrical length and impedance profile. This state-dependent variability in the network topology makes achieving a consistent, wideband impedance match for arbitrary antenna pairs practically infeasible.

3.3.3 Solution: Circulator-Based Switching Fabric. To overcome the pitfalls of the bus approach, we designed a circulator-based RF switching fabric that ensures stable impedance and clean isolation between every transmit and receive path. Figure 6 shows the architecture for a four-antenna example. The design incorporates a *three-port RF circulator* at each antenna, a non-reciprocal device that permits signal flow in only one direction (e.g., from port 1 to 2, and 2 to 3). This property is key to creating one-way signal paths and decoupling transmit and receive streams.

In our design, each antenna is connected to port 2 of its dedicated circulator. Incoming signals from the antenna always exit via port 3, while outgoing signals to the antenna are injected at port 1. This hardware-level separation ensures that a transmit signal cannot leak back into the receive network, and a received signal cannot interfere with other transmit circuits. Building on this isolation, we introduce three switching components. A multi-throw *receive switch* selects the port 3 output from any antenna's circulator. A *transmit switch* routes an input signal to the port 1 input of any desired antenna's circulator. Finally, a *mode switch* toggles the fabric's function by either connecting the receive switch output to the transmit switch input for signal forwarding (*forwarding mode*) or to a power detector for signal sensing (*sensing mode* detailed in §3.3.4). These components are realized with off-the-shelf wideband RF switches, each exhibiting low insertion loss of approximately 0.5-1 dB.

This architecture creates topological stability. Unlike the bus, where inactive elements disrupt active path, the circulator-based design renders inactive antennas electrically invisible to the selected signal path. Each connection is a clean cascade of well-matched, unidirectional components, presenting a stable impedance regardless of which antenna pair is chosen. The fabric can thus reconfigure connections on demand without impedance re-tuning. In summary, our circulator-based fabric provides the desired any-to-any flexibility with strong isolation and predictable RF behavior, enabling low-loss, stable links between any chosen antenna pair.

3.3.4 Built-In Angle-of-Arrival Estimation. A key capability of our circulator-based fabric is its inherent support for real-time, hardware-accelerated angle-of-arrival (AoA) estimation. This functionality is a direct consequence of the Luneburg lens's fundamental focusing property, which concentrates an incoming plane wave from a given direction onto a specific focal point on the lens's surface, where an antenna element is located. Our control circuit exploits this principle by operating the fabric in its *sensing mode*.

The estimation process is straightforward and efficient. The *receive switch* sequentially connects the output of each antenna's circulator (port 3) to a single, common RF power detector. By rapidly cycling through all antennas and measuring the received power at each, the system performs a hardware-based spatial search across its entire field-of-view. The antenna that registers the maximum power reading directly corresponds to the signal's angle of arrival.

This mechanism offers two key advantages over conventional approaches. First, it determines the source direction without requiring complex digital signal processing or any prior knowledge of the transmitter's location, addressing a major limitation of traditional RIS-based systems. Second, the lens provides sharp energy focusing, creating strong power contrast between the peak antenna and its neighbors for clear direction finding. This low-overhead, real-time AoA sensing is the critical enabler for OrbWeaver's efficient beam alignment protocol, which decomposes the complex three-node alignment problem into simpler, independent subproblems, as detailed in the next section.

3.4 Composable Operation Modes

The power of the OrbWeaver architecture lies in its inherent modularity and the composability of its core hardware primitives. By reconfiguring the signal paths through these primitives in software, a single, unified OrbWeaver platform can be composed into a variety of sophisticated operation modes, as detailed below.

Reflective Mode. A single *OrbWeaver unit*, *i.e.*, the lens, the antenna array and the RF switching fabric, can function as a programmable, high-gain reflective surface for arbitrary 3D beam steering, as shown in Figure 2(c). In this configuration, the Luneburg lens focuses an incident plane wave onto a specific antenna element corresponding to its angle of arrival. The backend switching fabric, operating in *forwarding mode*, is configured to route the captured signal from this receive antenna to any other designated transmit antenna on the same hemispherical array. This mechanism of steering via feed selection provides consistent, high-gain beams across a full 3D field-of-view, fundamentally avoiding the scan loss penalty that limits the effective coverage of conventional planar metasurfaces.

Transmissive Mode. The architecture can be extended to create a steerable, end-to-end link that effectively penetrates physical obstacles. As shown in Figure 7, this is achieved by composing two OrbWeaver units, typically placed on opposite sides of a barrier like a wall. The first unit captures the incoming signal, and its switching fabric routes it to the second unit. The second unit's fabric then injects this signal into a chosen transmit antenna, which radiates a collimated beam toward the final destination. A key advantage of this composition is that the input and output beam directions are fully decoupled, allowing them to be steered independently by their respective control circuits.

Multi-Beam and Multi-User Scaling. The OrbWeaver architecture naturally scales to support multi-beam and multi-user scenarios, where a single incident signal must be redirected to multiple, spatially distinct receivers. This composition, shown in Figure 8, is realized by using a passive RF power splitter to fan out the signal received by an input OrbWeaver unit to two or more output units. Crucially, each output unit retains full, independent control over its outgoing beam direction via its local switching fabric. The high isolation inherent in the circulator-based design (§3.3.3) ensures that reconfiguring one output beam does not create impedance mismatches or interference that would degrade the performance of the others.

Takeaway. Thanks to its modular lens-plus-fabric design, OrbWeaver flexibly realizes all three modes with the same hardware, offering functional versatility comparable to planar RIS platforms within a single, unified architecture. The extensibility of these architectural principles suggests the potential for developing additional, more sophisticated compositions beyond the operational modes demonstrated herein.

3.5 Beam Alignment and Tracking

Efficient beam alignment is a fundamental prerequisite for establishing and maintaining high-gain directional links, particularly in mmWave and other high-frequency bands. The introduction of an intermediate reconfigurable surface, such as OrbWeaver, transforms the standard two-party alignment problem into a more complex multi-node problem.

Curse of Dimensionality. Consider a three-node communication link consisting of a transmitter, a receiver, and an intermediate reconfigurable surface. Each node can steer its beam across a continuous range of angles. Let θ_t, ϕ_r, ϕ_t, and θ_r denote the beam angles for the transmitter, the surface's receive side, the surface's transmit side, and the receiver, respectively. The objective is to find the tuple of

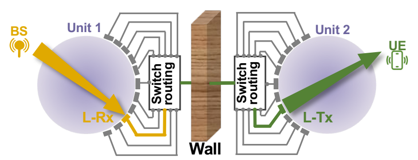

Fig. 7 – Transmissive mode operation. Two paired OrbWeaver units route a signal through a physical barrier, with the first capturing the signal and the second steering it to the user.

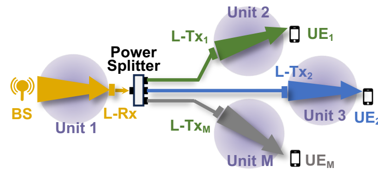

Fig. 8 – Scale to multi-units. A power splitter directs an incoming signal to multiple output units, enabling independently steered beams to serve several users simultaneously.

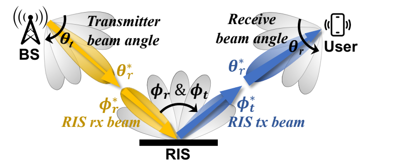

Fig. 9 – Conventional RIS beam alignment. A standard RIS requires a complex joint optimization of the transmitter, receiver, and both surface angles, which creates significant overhead.

angles $(\theta_t^*, \phi_r^*, \phi_t^*, \theta_r^*)$ that maximizes a link quality metric, Q (*e.g.*, received signal strength (RSS) or signal-to-noise ratio (SNR)), at the receiver. The joint optimization problem is:

$$(\theta_t^*, \phi_r^*, \phi_t^*, \theta_r^*) = \underset{\theta_t, \phi_r, \phi_t, \theta_r}{argmax}\, Q(\theta_t, \phi_r, \phi_t, \theta_r) \quad (2)$$

The core challenge lies in the deep coupling of these four variables; the end-to-end link quality is a function of the entire cascade, and evaluating Q requires a physical measurement over the complete path, *at the receiver.*

Baseline 1: Direct Two-Node Alignment. In a conventional system without an intermediate surface, the problem simplifies to a two-dimensional search over transmitter beam angle θ_t and receiver beam angle θ_r. A standard exhaustive search involves the transmitter sweeping its beam across all possible angles while the receiver does the same for each transmitter angle. To quantify this overhead, if the search space is discretized into n distinct directions, this requires $n \times n$ measurements, yielding a complexity of $O(n^2)$.

Baseline 2: Conventional RIS-Assisted Alignment. The introduction of a conventional RIS, a passive device with no inherent sensing or measurement capabilities, escalates the problem significantly. Because the conventional beam-scanning-based RIS itself cannot measure signal strength, the only point in the system capable of evaluating the quality function Q remains the final receiver. Consequently, for every possible configuration of the Tx-RIS-Rx path, a full end-to-end measurement is required. As illustrated in Figure 9, for an equivalent search resolution of n directions at each node, this complexity scales as $O(n^4)$.

Baseline 3: RIS-Assisted Alignment with Assumptions. To mitigate the prohibitive $O(n^4)$ complexity, many existing works [10, 22, 58, 59] simplify the problem by assuming a static topology: the relative position between transmitter and RIS do not change after an initial deployment. A single, costly exhaustive search $O(n^4)$ is performed once to establish the optimal TX-to-RIS beam pair (θ_t^*, ϕ_r^*). Subsequently, the alignment problem is reduced to a more manageable search over the RIS-to-RX link. However, this assumption is exceedingly fragile in practice. It fails whenever the RIS is mobile (*e.g.*, mounted on a vehicle or drone) or when the environment is dynamic, such as when the LOS path between the transmitter and RIS is temporarily occluded by moving people or objects. In any such scenario, the established TX-RIS link is invalidated, forcing a complete system-wide rescan that reverts to the full overhead.

3.5.1 Decoupled Alignment via In-Situ Sensing. The OrbWeaver architecture overcomes the prohibitive complexity of joint beam alignment by fundamentally changing the problem's structure. Our key idea is to leverage the hardware capabilities introduced in §3.3.4 to decouple the four-dimensional search into two independent, sequential two-dimensional searches. This is enabled by OrbWeaver's ability to perform *in-situ* signal strength measurements.

The circulator-based switching fabric, with its distinct *mode switch*, allows OrbWeaver to toggle between a standard *forwarding mode* and a unique *sensing mode.* In sensing mode, the *receive switch* routes the signal from a selected antenna not to the transmit chain, but to an integrated RF power detector. This provides a mechanism for local, hardware-accelerated AoA estimation, breaking the reliance on the end-receiver for the first half of the alignment process. This leads to a two-stage protocol, detailed as follows.

Stage I (Tx to Surface): The transmitter sweeps its beam across all possible angles while sending a pilot signal. Concurrently, OrbWeaver, operating in sensing mode, sweeps its receive beam angle using its *receive switch.* For each pair of transmit and receive angles (θ_t, ϕ_r), the onboard detector measures the local RSS. The angle pair that maximizes this local metric is selected. This stage involves a two-dimensional search over the Tx and surface-receive angles, with a complexity of $O(n^2)$ for an equivalent discretized search space.

Stage II (Surface to Rx): Once the optimal incoming path is found, OrbWeaver's controller fixes the receive angle and toggles the *mode switch* to forwarding mode. The transmitter now uses its determined optimal angle. OrbWeaver then sweeps its outgoing beam angle using the *transmit switch*, while the receiver simultaneously sweeps its own beam angle to find the pair that maximizes the end-to-end RSS. This stage requires a two-dimensional search over the surface-transmit and Rx angles, with a complexity of $O(n^2)$.

Complexity Reduction. Without *making any assumptions of the topology*, our protocol transforms the multiplicative complexity of a joint four-dimensional search $O(n^4)$ into an additive complexity of two sequential two-dimensional searches $O(2 \cdot n^2)$, a dramatic reduction in search space.

3.5.2 Low-Overhead Mobility Tracking. In mobile scenarios, the optimal beam direction changes continuously, necessitating frequent realignment. The high overhead of conventional schemes makes them ill-suited for tracking mobile users, often causing link degradation or failure. OrbWeaver's architecture provides a natural and highly efficient solution.

The key principle is that user mobility typically causes gradual changes in the AoA at the surface. The new optimal receive beam is highly likely to be in the immediate vicinity of the previously optimal one. Instead of re-initiating a global search, OrbWeaver can leverage its low-cost sensing capability to perform frequent, localized tracking. The protocol is simple: OrbWeaver periodically re-enters sensing mode for a very brief interval to perform a local search. The *receive switch* scans only a small neighborhood of antennas around the last-known optimal port (e.g., the best port $\pm k$ neighbors). This local AoA update is extremely fast and, critically, can be performed autonomously by the surface without requiring any feedback from the end-receiver, a significant advantage over traditional architectures that must re-evaluate the entire end-to-end link in response to any change.

4 IMPLEMENTATION

Millimeter-Wave Transceivers. For controlled experiments, we employ two USRP 2954R [60] software-defined radios equipped with UBX-160 daughterboards that serve as intermediate frequency transceivers operating from 2–6 GHz. These are coupled with two frequency converters to generate and process mmwave signals in 26.5 - 29.5 GHz range.

Luneburg Lens. We fabricate a spherical Luneburg lens using commercial 3D printing services with LEDO 6060 SLA photopolymer. Figure 2(b) shows the printed lens assembled from cubic structures. The 28 GHz lens has a 39 mm radius and costs approximately $6.5, including printing and materials. We also print a 5.8 GHz lens with a 154 mm radius using 14 mm cubes (parameter *a*) and 2 mm rods (parameter *c*). This approach readily scales to other frequencies by adjusting cube size, and commercial 3D printers can achieve resolutions down to tens of micrometers.

Hemispherical Antenna Array. The hemispherical antenna array are consist with several patch antennas using Rogers 5880 dielectric substrates with a relative permittivity of 2.2. The first layer is 0.508 mm thick, and the second and third layers are 0.254 mm thick. The overall element size is 5.45×5.45 mm, with a radiation patch size of 2×1 mm and a feedline size of 1×1 mm. To ensure the antenna elements cover the hemisphere of the Luneburg lens, we fabricated a custom support structure using 3D printing to fix the array element positions as shown in Figure 10(a) and Figure 10(b). During evaluation, only 16 antenna elements are used.

Antenna Element Control Circuit. To rapidly build a proof-of-concept covering sub-6 GHz to 30 GHz, we use readily available commercial off-the-shelf (COTS) components, as shown in Figure 10(c). The 16-port design integrates four SP8T switches [61], three SPDT switches [61], one envelope detector (ADL6010Evalz [62]), and sixteen circulators [63]. By replacing these components with functionally equivalent RF integrated chips (e.g., MA4AGSW8-1 [64], ADRF5020 [65]) and assembling them on PCB, the overall cost can be substantially reduced while maintaining ultra-wideband performance. Further cost reduction is achievable when using RF ICs optimized for specific frequency bands.

5 EVALUATION

In this section, we present a comprehensive performance evaluation of OrbWeaver across multiple dimensions. We first establish the fundamental system characteristics through microbenchmarks that quantify key parameters, including focusing capability, system operating bandwidth, and other critical specifications (§5.1). Then we evaluate the end to end performance by measuring the signal-to-noise ratio (SNR) improvement in reflective, transmissive modes and mobility scenarios(§5.2). To evaluate system robustness, we characterize beam-steering performance under varying operational conditions, examining the effects of Tx-unit distance, incident beam angles, and power levels (§5.3). We further demonstrate real-world performance using off-the-shelf base stations and user equipment (§5.4) then evaluate the system's scalability to sub-6 GHz operation (§5.5). Finally, we perform a head-to-head comparison between OrbWeaver and state-of-the-art planar RIS designs in terms of coverage, power, latency, and beam alignment complexity (§5.6)

5.1 Microbenchmarks

In our microbenchmark, we evaluate OrbWeaver's physical-layer characteristics, including lens properties, system bandwidth, circuit-related performance such as insertion loss and AoA measurement ability.

Incident Beam Concentration Performance. To evaluate the receive-side convergence capability of the lens, we conduct distance-varying measurements by placing the lens directly in front of the receiver. As illustrated in Figure 11(a), we vary the distance between the lens and the transmitter (Tx) from 3 m to 18 m while measuring the received RSSI at the receiver (Rx). By comparing the SNR measurements with and without the lens, we assess the focusing gain provided by the lens. The results demonstrate that a single-lens configuration achieves SNR improvements ranging from 11 dB to 33 dB across all the distances.

(a) Patch Ant. (b) Lens shell. (c) Control circuit. (d) COTS 5G station. (e) Corner scenario. (f) Through-wall scenario.

Fig. 10 – OrbWeaver hardware implementation and deployment scenarios.

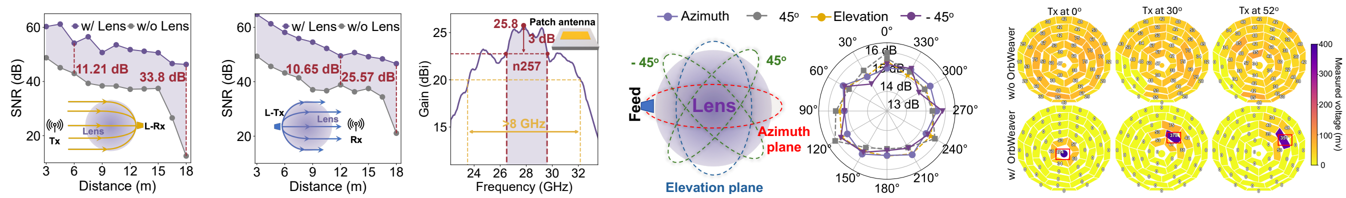

(a) Lens enhanced convergence SNR gain. (b) SNR Gain from Lens Concentration. (c) System bandwidth evaluation result. (d) Lens isotropy: Test geometry schematic (left). Multi-plane gain patterns (right). (e) AoA capability validation: Without lens (top) compared to with lens (bottom).

Fig. 11 – OrbWeaver micro-benchmark performance.

Transmit Beam Concentration Performance. To assess the transmit-side convergence, we position the lens in front of the Tx, as shown in Figure 11(b). The receiver is moved from 3 m to 18 m while we measure the RSSI at each position. The results indicate that, compared to the baseline configuration without the lens, our system achieves SNR improvements of 10–25 dB across all the tested distance range. The results confirm the lens's capability to concentrate transmitted power into a more directional beam, increasing the signal strength at the receiver location.

System Bandwidth Evaluation. Since the lens can only converge or concentrate waves, it cannot work independently. Therefore we define our system bandwidth as that of the patch antenna with the lens in front. We evaluate the system bandwidth in an anechoic chamber through vector network analyzer (VNA) measurements. The transmitter is a standard gain horn connected to Port 1 of the VNA sweeping from 22 to 34 GHz. The receiver at VNA Port 2 alternates between our lens–antenna and a standard gain horn for reference. By normalizing the measured response against the reference horn's known gain, we determine the absolute gain of the patch antenna with the lens. As shown in Figure 11(c), OrbWeaver maintains a gain above 20 dBi across the frequency range of 23.6–32.1 GHz (>8 GHz). Within the 3GPP n257 band (26.5–29.5 GHz), OrbWeaver exhibits consistently high performance with gain remaining above 23 dBi and a peak of 25.8 dBi. The results confirm the OrbWeaver's suitability for wideband mmWave communication.

Lens Isotropy Validation. For a 3D programmable ball, the lens's isotropy is important to our system since it ensures uniform performance regardless of the Tx's spatial position, which is critical for reliable communication links in dynamic environments. To examine the isotropy of our system, we place a feed antenna at the focal point of the lens and measure the radiated beam pattern by rotating the lens in 30° increments across 360° in the azimuth and elevation planes as well as two diagonal planes at ±45° (Figure 11(d)). The received power is recorded at each orientation. The results show minimal gain variation across all measured angles (typically within 1 - 2 dB), confirming that OrbWeaver lens exhibits good isotropic performance.

Circuit Validation. To validate our backend circuit performance, we conduct two complementary evaluations: insertion loss characterization and AoA measurement capability.

(a). Insertion Loss of Switching Circuit. We systematically measure the insertion loss of all circuit components to quantify the overall system loss budget. The measured insertion losses of each component are all less than 1 dB, specifically 0.9 dB for the SP8T switch and 0.8 dB for the SPDT switch. Each patch antenna element is connected to one circulator, with each circulator contributing 0.5 dB of loss. The total insertion loss is 5.2 dB for the 16-output circuit.

(b). AoA Measurement Validation. Our system inherently supports signal convergence and AoA sensing. Each backend antenna corresponds to a specific AoA of the incident wave. By sequentially activating each antenna, we can identify the Tx's direction by detecting which antenna collects the strongest signal. To validate this capability, we fix the Tx at a constant distance and vary its angle to 0°, 30° and 52°. We then measure received power across all backend antennas under both with-lens and without-lens conditions. As shown in Figure 11(e), the lens enables concentrated high-power regions aligned with the incident angles, confirming effective signal focusing and accurate AoA detection. Without the lens, power spreads across most antennas, resulting in poor directional convergence and degraded AoA resolution.

To evaluate Tx AoA estimation accuracy, we place the Tx at 33 locations from −80° to 80° with 5° intervals. At each

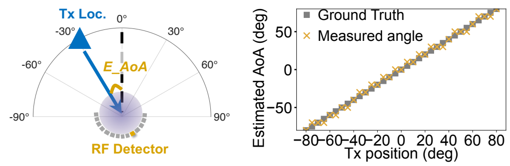

(a) AoA test scenario. (b) Estimated AoA result.

Fig. 12 – Evaluation of Tx beam AoA accuracy.

position, the system performs channel-switching energy detection and selects the antenna element with the maximum received power based on ADC samples. The angle between this element and the lens center (relative to the 0° axis) is reported as the estimated AoA. During the experiment, the Tx is always facing lens just as shown in Figure 12(a). Figure 12(b) shows that OrbWeaver accurately estimates the AoA when the incident angle is an integer multiple of 10°. However, when the angle falls between these values (e.g., 5°, 15°, 25°), the estimate may deviate by up to ±5°. This limitation stems from the 10° angular spacing of the antenna array behind the lens. A detailed analysis is provided in Appendix A.

5.2 End-to-End Performance

We evaluate the end-to-end performance of OrbWeaver across reflective mode, transmissive mode, and mobility scenarios. To quantify performance, we measure the received signal SNR at different positions repeatedly and average the results.

Reflective Mode with One Unit. To validate the beam-steering capability of our system in the reflective mode, we conduct experiments in a corridor environment (Figure 10(e)). The unit is positioned at a corner, creating a non-line-of-sight (NLoS) configuration between the Tx and the Rx. The Tx is placed 4 m away from the unit, while the Rx is deployed at 20 distinct spatial points along the corridor.

As shown in Figure 13, without OrbWeaver most Rx positions experience SNR levels below 20 dB, with only five locations exceeding this threshold. In contrast, with OrbWeaver all Rx positions achieve SNRs above 21 dB, with the maximum reaching 27.8 dB including those around the corner. Although multipath effects cause smaller SNR gains at certain locations, the unit consistently enhances the dominant incoming path, resulting in SNR improvement across all receiver positions and demonstrating that OrbWeaver remains robust to multipath in this NLoS scenario.

Transmissive Mode with Two Units. We further evaluate the beam-steering performance of OrbWeaver in a through-wall scenario (Figure 10(f)). The Tx and Rx are placed outdoors and indoors, respectively, with the LoS path completely blocked by a wall. As shown in Figure 14, we position unit 1 outdoors and unit 2 indoors, with their backend circuits connected via RF cables routed through a window. The Tx is positioned 4 m away from unit 1, while the Rx is deployed at 29 locations spanning an angular range from −80° to 80°.

Figure 14 shows the measured SNR values before and after deploying OrbWeaver. Without OrbWeaver, most measured SNR at Rx locations are below 20 dB due to the strong isolation of the wall. With OrbWeaver enabled, all Rx positions achieve SNRs of at least 28 dB. The SNR gains range from 5 dB to 27 dB across all positions including corners. These results show that OrbWeaver can restore link quality and expand mmWave coverage across walls, and it is suitable not only for indoor deployments with structural blockages but also for outdoor-to-indoor communication scenarios.

Mobility Scenario with Tx/Rx Movement. To validate the robustness and programmability of our system, we evaluate two scenarios in transmissive mode: one with the Tx moving and the other with the Rx moving. The Tx continuously transmits signals while the Rx records the received SNR over 10 repeated trials. Each trial lasts 800 ms, including 230 ms for switch polling and 570 ms for data transmission.

For the Tx mobility scenario, the Rx is fixed 3.5 m away from unit 1 at 90° in the azimuth plane. The Tx is placed 3 m from the unit 2 and moves from −30° to +45° relative to unit 2. We test three different moving speeds: 0.5 m/s, 1.0 m/s, 1.5 m/s. During polling, the system sequentially activates antenna channels to detect the incoming direction. The test result is shown in Figure 17(a). Under Tx mobility, the received SNR with our system remains above 38 dB across all speeds, while the baseline without the system stays around 20 dB. Even at the highest speed of 1.5 m/s, the average link margin remains about 15 dB. The temporary dips correspond to polling intervals when the system is probing directions.

For the Rx mobility scenario, the Tx is fixed at 3 m away from unit 1 and at 90° in the azimuth plane, while the Rx moves across the same angular range and speeds. The active transmit channel of unit 2 is dynamically updated according to Rx feedback. As shown in Figure 17(b), our system provides more than 10 dB gain over the baseline without OrbWeaver across all movement speeds. Unlike the Tx mobility scenario, unit 2 continues communication during polling, so no significant fluctuations are observed.

5.3 Impact of System Parameters

This section investigates how various parameters, including the transmit power, Tx-unit distance and incident angle of the signal source, influence system performance.

Transmit Power. We first examine whether OrbWeaver's performance depends on the incident power. The positions of the transmission antenna, unit and Rx are fixed, with the Tx-unit and unit-Rx distances both set to 4 m. The transmission output power is varied from 0 to 14 dBm. As shown in Figure 15, the SNR improvement remains nearly constant across all Tx power levels, ranging from 20.4 to 22.4 dB.

Tx-unit Distances. We evaluate the impact of Tx–unit separation on system performance. The Rx is fixed 3.5 m from the

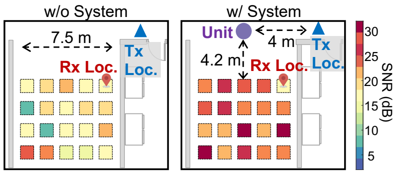

Fig. 13 – SNR gain enhancement through reflective mode.

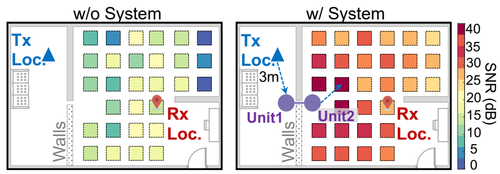

Fig. 14 – SNR gain enhancement in transmissive mode operation.

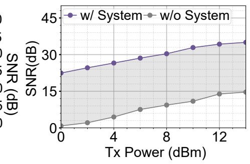

Fig. 15 – Transmitter power effect.

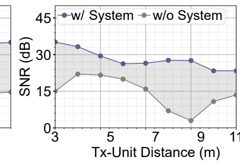

Fig. 16 – Tx-Unit distance impact.

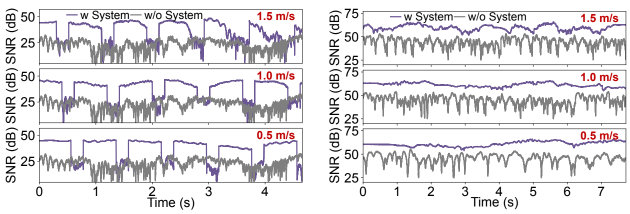

(a) Tx moving.

(b) Rx moving.

Fig. 17 – SNR enhancement when the Tx or Rx moves.

unit at 45°, while the Tx is placed along the −45° direction with its distance varied from 3 to 11 m in 0.5 m steps. As shown in Figure 16, OrbWeaver consistently outperforms the baseline across all distances, achieving 10–15 dB SNR improvement. The results are stable, with minor fluctuations due to indoor multipath, including a dip around 7–9 m.

Incident Beam Angles. We evaluate the impact of different incident angles on both reflective and transmissive modes. The Tx is positioned 2.5 m from the unit at azimuth angles of 0°, −30°, and 60°, and elevation angles of 30°, −30°, and 60°. The Rx is sequentially moved across 17 positions from −80° to 80°. We calculate the SNR gain compared without OrbWeaver. The results are shown in Figure 18(left) for reflective and in Figure 18(right) for transmissive modes respectively.

In reflective mode, the SNR gain varies significantly with incident angle, ranging from a maximum of 26.3 dB to a minimum of 5.6 dB. The overall gain is lower than in transmissive mode, particularly when the Tx is at −30° and the Rx at −40°. In this configuration, the Tx and Rx are nearly aligned, resulting in a strong direct signal that diminishes the relative improvement provided by OrbWeaver. In contrast, transmissive mode exhibits higher and more stable performance. With the wall providing Tx–Rx isolation and thus a naturally low noise floor, OrbWeaver consistently achieves gains above 30 dB across all the incident angles, with variations of 2.78–5.32 dB across different Rx angles.

5.4 User Case I: Commercial mmWave 5G

We validate the practicality of our design on a commercial 5G mmWave platform consisting of an off-the-shelf base station (BS) [66] and two commodity user equipments (UEs) [67], as shown in Figure 10(d). The BS is configured to transmit a single synchronization signal block (SSB) with a fixed beam towards the unit, and the received SSB is routed by the unit to the target UE. We evaluate system performance using the UE-reported reference signal received power (RSRP) and end-to-end throughput.

Reflective Mode. We place a UE at each of eight non-line-of-sight (NLoS) locations created by a corner blocking the direct path from the BS (Figure 19(a)). The unit redirects the incident mmWave signal toward the shadowed UEs, and as shown in Figure 19(b), it achieves an RSRP gain of 5–10 dB, resulting in throughput improvements of 160-380 Mbps compared to the baseline without the OrbWeaver unit.

Transmissive Mode. In this case, the BS is deployed outdoors while the UE is placed indoors. They are separated by a wall that blocks the direct path, just as shown in Figure 19(c). By focusing and forwarding the incoming beam, OrbWeaver enhances the received signal by at least 5 dB and up to 20 dB. This results in throughput improvements of at least 167 Mbps and up to 430 Mbps (Figure 19(d)).

Multi-user Scalability. We place the BS outdoors and two UEs indoors in separate regions divided by absorbing walls to set up a multi-user scenario (Figure 19(e)). A power splitter is connected with dual units to simultaneously route the beam to both UEs. The result is shown in Figure 19(f). Compared with the case without our system, both users experience enhanced RSRP ranging from 15–21 dB and stable throughput up to 265.3 Mbps. For the positions (P4 and P5 of UE1) where the user lost the connection, our system is able to recover the link and maintain a stable throughput. This configuration eliminates the need for a circulator, thereby avoiding 1 dB loss, while introducing an additional 4 dB per-branch loss due to the theoretical 3 dB power split and less than 1 dB insertion loss of the power divider. Despite this additional loss, the proposed system still provides substantial performance gains compared to the baseline without our system. Furthermore, as illustrated in Figure 8, the three units are driven by independent but identical control circuits, each performing beam steering locally without inter-units coordination, thereby introducing no additional control complexity compared to the single-unit configuration.

5.5 User Case II: sub-6 GHz WiFi

In this section, we implement OrbWeaver at 5.8 GHz and evaluate it on a commercial WiFi platform. We follow the design and fabrication procedures in §3.1 and §3.2 to construct a lens with a 15.4 cm radius and a 52 mm × 32 mm patch antenna array. We then evaluate its beam-steering performance

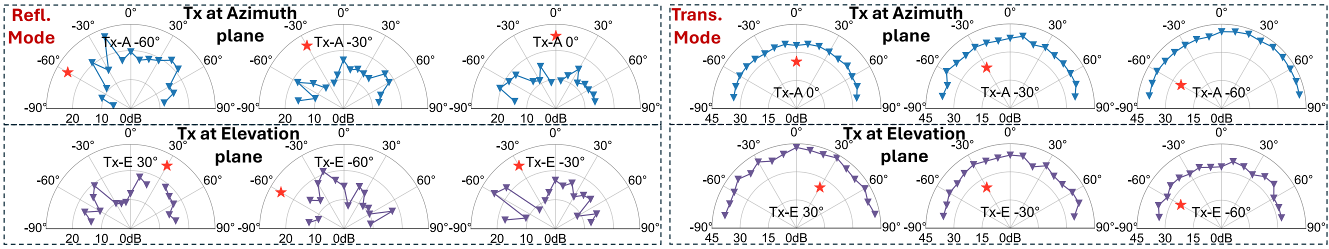

Fig. 18 – Incident beam angles under different planes: Tx is positioned in the azimuth (A) and elevation (E) planes for reflective mode (left) and transmissive mode (right). The transmitter is marked with a red star, and the receiver is measured at different angles from −80° to 80° with the angular resolution of 10°.

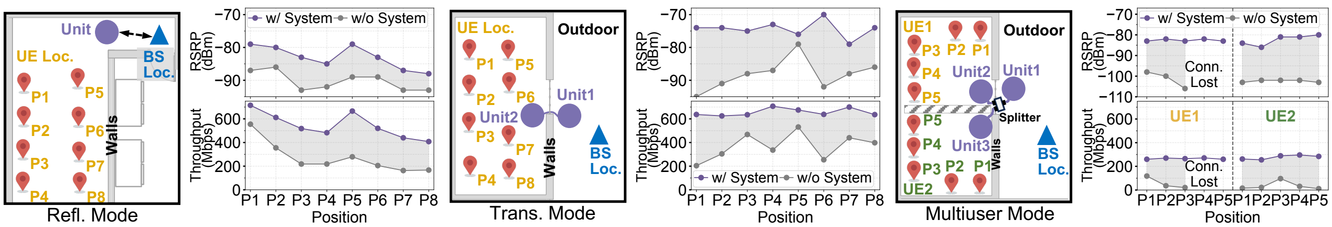

(a) Refl. scenario. (b) RSRP & throughput gains. (c) Trans. scenario. (d) RSRP & throughput gains. (e) Multiuser. (f) RSRP & throughput gains.

Fig. 19 – Real-world validation on 5G mmWave base station under varied modes.

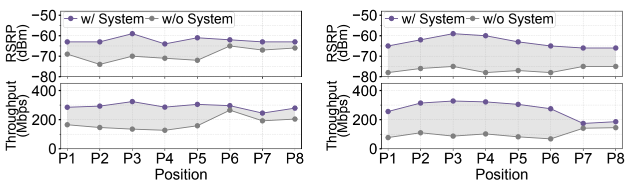

(a) Reflective mode. (b) Transmissive mode.

Fig. 20 – Measured RSS and throughput validation of OrbWeaver on a commercial WiFi platform.

in both reflective and transmissive modes. We use the same reflective and transmissive scenarios as in User Case I. A 5.8 GHz commercial WiFi router [68] serves as the transmitter and a smartphone as the UE. We measure throughput and RSS using a speed test application [69].

Reflective Mode. We block the LoS between the router and the UE. The UE is sequentially moved to different positions to measure the RSS and throughput. The result is shown in Figure 20(a). Compared with the case without OrbWeaver, the received signal SNR improves by 3.5–11 dB and the communication throughput increases by 31–189 Mbps.

Transmissive Mode. For the transmissive mode, the router is moved outdoors. Since the wall provides limited attenuation, we add additional absorber material to block the signal between the router and the UE. As shown in Figure 20(b), the received SNR increases by 16–23 dB, while the communication throughput improves by 33–241 Mbps.

5.6 Comparison with Planar RISs

In this section, we conduct a comprehensive head-to-head evaluation against planar RISs in terms of coverage, latency, power consumption, and system complexity.

Coverage. To evaluate 3D coverage, we deploy OrbWeaver and the planar RIS developed by RF-Bouncer [40] (size 0.35m× 0.35m with 16 × 16 elements) at the same location and perform identical measurements. With the transmitter fixed (1 m from the RIS at 0° incidence), we measure the SNR improvement over angles from −85° to +85° in both horizontal and vertical planes. Figures 21(a) and 21(b) show that OrbWeaver achieves consistently high and stable SNR gain across the full angular range in both planes, with gains of 20–27 dB horizontally and 18.9–29 dB vertically, and less than 7 dB variation. In contrast, the planar RIS provides comparable gain only within ±60°, beyond which the SNR enhancement degrades sharply, dropping to below 5 dB at extreme angles.

Overall, OrbWeaver provides substantially wider angular coverage. This advantage stems from its spherical lens geometry, which enables wide-angle 3D beamforming, making OrbWeaver well suited for IoT scenarios where devices are placed arbitrarily in complex indoor environments.

Latency. The latency of RF-Bouncer is mainly determined by codebook switching, with a minimum of 10 ns. The latency of OrbWeaver depends on RF switch transition time. Our proof of concept uses mechanical switches with a 10 ms switching time to validate functionality across sub-6 GHz and mmWave bands. By integrating commercial electronic switch chips such as MA4AGSW8-1 [64] and ADRF5020 [65], with switching times as low as 20 ns, scanning all antennas would take less than 2.8 μs. As the dwell time in 5G NR beam management is 18 μs, OrbWeaver enables real-time, protocol-compliant beam alignment within existing standards.

Power. We measure power consumption using an HV power monitor. For RF-Bouncer, power is primarily consumed by

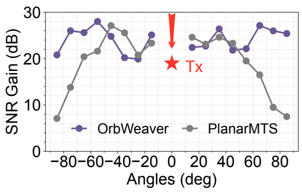

(a) Horizontal Plane.

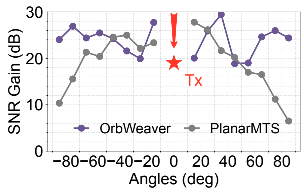

(b) Vertical Plane.

Fig. 21 – Measured SNR gain at different angles comparing OrbWeaver and planar RIS w/ and w/o the system.

512 PIN diodes, the MCU, and 64 shift registers, resulting in an average of 3.33 W. In contrast, OrbWeaver's power mainly arises from four SP8T switches, three SPDT switches, and the MCU, with an average consumption of 3.87 W in the current prototype. With an optimized integrated PCB design, the total power consumption can be reduced to 159 mW in sensing mode and 450 mW in forwarding mode.

Hardware Complexity. Planar RIS designs rely on per-element phase tuning using dense diode-based control networks, whereas OrbWeaver adopts a switch-based directional control architecture. In RF-Bouncer, 512 diodes are integrated on the metasurface to control the phase of each unit, which requires the MCU to provide at least 512 I/Os for control. In contrast, OrbWeaver only needs 4 SP8Ts, 3 SPDTs and 16 passive circulators to achieve control in 16 directions. This architectural shift eliminates the need for per-element biasing and high-fanout control interfaces. The significantly reduced number of hardware components can lower the system control complexity. Furthermore, the limited number of active components, combined with the PCB integration of RF chips, results in a total cost of $144 for the same frequency band, whereas the RF-Bouncer costs approximately $246. Consequently, the hardware and control complexity of OrbWeaver scales with the number of directions rather than the number of metasurface elements.

Beam Alignment Complexity. Existing beam-scanning based RIS systems (e.g., mmWall [10], NR-Surface [20], RF-Bouncer [40]) must align the BS transmit beam, RIS receive and reflect directions, and UE receive beam, leading to a beam alignment complexity of $O(n^4)$. ScatterMIMO [41] lowers the overhead to three packets ($O(1)$) by leveraging precise differential channel estimation, which is highly sensitive to random phase offsets and multipath variations. It further assumes that the AP and RIS know each other's positions and that UE packets can be surface-modulated and received by the AP. This requirement implies that both AP and UE antennas must be omnidirectional or have wide beams, which is impractical for mmWave frequencies that rely on narrow-beam transmission. In contrast, OrbWeaver maintains a consistent $O(n^2)$ complexity without relying on prior location knowledge or static link assumptions, providing the scalability and robustness required for dynamic wireless environments.

6 DISCUSSION

Design Trade-offs and Future Integration. The current prototype uses off-the-shelf SP8T switches and circulators to enable flexible experiments across sub-6 GHz and mmWave bands without band-specific redesign. This modular design enables rapid validation of the spherical metasurface concept across multiple frequencies. For deployment, the control circuitry can be further optimized through integration. Replacing discrete components with chip-level integrated switches and band-specific circulators would reduce cost, shrink form factor, and lower power consumption.

Transmissive Mode Feasibility. The transmissive mode targets scenarios where RF penetration is severely attenuated or impossible, such as between adjacent rooms separated by concrete or metallic partitions. In such cases, a short cable relay is practical and commonly used in infrastructure installations. Here, the cable serves merely as a short passive conduit, while the two lenses handle beamforming and redirection. This architecture enables NLoS coverage extension through obstacles that wireless-only RIS cannot penetrate.

Deployment Considerations. First, due to the hemispherical arrangement of the antenna array, effective gain is limited to the front 180° FoV. Deployments must ensure that the BS and UE are located within this coverage zone. Second, the Tx–lens distance is mainly constrained by the detector's sensitivity, allowing reliable sensing only when the received signal exceeds the detection threshold. In our prototype, with a sensitivity of −35 dBm and a transmit power of 14 dBm, a stable sensing range is achieved up to 15 m. The distance can be extended by improving the detector sensitivity.

7 CONCLUSION

This paper presents OrbWeaver, a new type of RIS that achieves low cost, simplicity, and true 3D coverage with only minimal control. Our design supports both reflective and transmissive modes, enabling versatile deployment across diverse scenarios. Through validation with a commercial 5G mmWave base station and a commodity sub-6 GHz WiFi platform, we demonstrate consistent improvements in both link gain and throughput. These results demonstrate the practicality of our design and open up new opportunities for deploying RIS technology in future wireless networks.

ACKNOWLEDGMENTS

This work is supported by the National Natural Science Foundation of China (62502384, W2511073) and the Key Research and Development Program of Shaanxi under Grants (2025GH-YBXM-057 and 2024GH-ZDXM-49). This work is also supported by Yaxiong Xie's startup funding. We thank our shepherd and anonymous reviewers for their insightful feedback which helped improve this paper.

References

[1] Theodore S. Rappaport, George R. MacCartney, Shu Sun, Hangsong Yan, and Sijia Deng. Small-scale, local area, and transitional millimeter wave propagation for 5g communications. *IEEE Transactions on Antennas and Propagation*, 65(12):6474–6490, 2017.

[2] Qing Xue, Chengwang Ji, Shaodan Ma, Jiajia Guo, Yongjun Xu, Qianbin Chen, and Wei Zhang. A survey of beam management for mmwave and thz communications towards 6g. *IEEE Communications Surveys & Tutorials*, 26(3):1520–1559, 2024.

[3] Lili Chen, Bozhong Yu, Ju Ren, Jeremy Gummeson, and Yaoxue Zhang. Towards seamless wireless link connection. In *Proceedings of the 21st Annual International Conference on Mobile Systems, Applications and Services*, pages 137–149, 2023.

[4] Sanjib Sur, Vignesh Venkateswaran, Xinyu Zhang, and Parmesh Ramanathan. 60 ghz indoor networking through flexible beams: A link-level profiling. In *Proceedings of the 2015 ACM SIGMETRICS International Conference on Measurement and Modeling of Computer Systems*, pages 71–84, 2015.

[5] Nozhan Hosseini, Mahfuza Khatun, Changyu Guo, Kairui Du, Ozgur Ozdemir, David W Matolak, Ismail Guvenc, and Hani Mehrpouyan. Attenuation of several common building materials: millimeter-wave frequency bands 28, 73, and 91 ghz. *IEEE Antennas and Propagation Magazine*, 63(6):40–50, 2021.

[6] L. Dai, B. Wang, M. Wang, X. Yang, J. Tan, S. Bi, S. Chen, and M.-S. Alouini. Reconfigurable intelligent surface-based wireless communications: Antenna design, prototyping, and experimental results. *IEEE Access*, 8:45913–45923, 2020.

[7] W. Tang, X. Chen, M.Z. Chen, J.Y. Dai, S. Jin, Y. Cheng, R. Zhang, and T.J. Cui. Path loss modeling and measurements for reconfigurable intelligent surfaces in the millimeter-wave frequency band. *IEEE Transactions on Communications*, 70(9):6259–6276, 2022.

[8] Michael Boyarsky, Timothy Sleasman, Mohammadreza F Imani, Jonah N Gollub, and David R Smith. Electronically steered metasurface antenna. *Scientific reports*, 11(1):4693, 2021.

[9] Kun Qian, Lulu Yao, Xinyu Zhang, and Tse Nga Ng. Millimirror: 3d printed reflecting surface for millimeter-wave coverage expansion. In *Proceedings of the 28th Annual International Conference on Mobile Computing And Networking*, pages 15–28, 2022.

[10] Kun Woo Cho, Mohammad H Mazaheri, Jeremy Gummeson, Omid Abari, and Kyle Jamieson. {mmWall}: A steerable, transflective metamaterial surface for {NextG}{mmWave} networks. In *20th USENIX Symposium on Networked Systems Design and Implementation (NSDI 23)*, pages 1647–1665, 2023.

[11] Yangfan Zhang, Yaxiong Xie, Zhihao Hui, Hao Jia, and Xiaojiang Chen. Hydra: Attacking ofdm-base communication system via metasurfaces generated frequency harmonics. In *Proceedings of the 30th Annual International Conference on Mobile Computing and Networking*, pages 938–952, 2024.

[12] Haoze Chen and Yasaman Ghasempour. Malicious mmwave reconfigurable surface: Eavesdropping through harmonic steering. In *Proceedings of the 23rd Annual International Workshop on Mobile Computing Systems and Applications*, pages 54–60, 2022.

[13] Yixin Cui and Linyan Guo. A frequency sensor of reconfigurable intelligent metasurface for 5g communication. In *2024 Photonics & Electromagnetics Research Symposium (PIERS)*, pages 1–7. IEEE, 2024.

[14] Fei Yang, Fan Xu, Chenxi Liu, Xinyu Yang, Ziqiang Wang, Junwei Wu, and Xiaojian Fu. Two-dimensional beam steering based on compact programmable coding metasurface. *Applied Sciences*, 12(22):11780, 2022.

[15] Wei Wang, Philip Lambert, and Jonathan Chisum. High-frequency limits for 3d-printed gradient-index (grin) lens antennas. In *2023 IEEE International Symposium on Antennas and Propagation and USNC-URSI Radio Science Meeting (USNC-URSI)*, pages 1695–1696, 2023.

[16] Nicolas C. Garcia and Jonathan D. Chisum. Compound grin fanbeam lens antenna with wideband wide-angle beam-scanning. *IEEE Transactions on Antennas and Propagation*, 70(9):7501–7512, 2022.

[17] Philip M. Lambert and Trevor Polidore. 3d-printed e-band gradient dielectric lens for automotive and industrial applications. In *2022 IEEE International Symposium on Antennas and Propagation and USNC-URSI Radio Science Meeting (AP-S/URSI)*, pages 2074–2075, 2022.

[18] Rudolf Karl Luneburg. *Mathematical theory of optics*. Univ of California Press, 1966.

[19] Xuanjing Li, Rui Feng, Quilin Tan, Jianjia Yi, Shixiong Wang, Feng He, and Shah Nawaz Burokur. Additively-manufactured broadband metamaterial-based luneburg lens for flexible beam scanning. *Materials*, 17(12):2847, 2024.

[20] Minseok Kim, Namjo Ahn, and Song Min Kim. Nr-surface: Nextg-ready μw-reconfigurable mmwave metasurface. In *NSDI*, 2024.

[21] Omid Abari, Dinesh Bharadia, Austin Duffield, and Dina Katabi. Enabling {high-quality} untethered virtual reality. In *14th USENIX Symposium on Networked Systems Design and Implementation (NSDI 17)*, pages 531–544, 2017.

[22] Tianxiang Li, Mohammad Hossein Mazaheri, and Omid Abari. Enabling on-demand low-power mmwave repeaters via passive beamforming. In *Proceedings of the 30th Annual International Conference on Mobile Computing and Networking*, pages 618–632, 2024.

[23] Kang Min Bae, Hankyeol Moon, Sung-Min Sohn, and Song Min Kim. Hawkeye: Hectometer-range subcentimeter localization for large-scale mmwave backscatter. In *Proceedings of the 21st Annual International Conference on Mobile Systems, Applications and Services*, pages 303–316, 2023.

[24] Suraj Jog, Jiaming Wang, Junfeng Guan, Thomas Moon, Haitham Hassanieh, and Romit Roy Choudhury. {Many-to-Many} beam alignment in millimeter wave networks. In *16th USENIX Symposium on Networked Systems Design and Implementation (NSDI 19)*, pages 783–800, 2019.

[25] Song Wang, Jingqi Huang, Xinyu Zhang, Hyoil Kim, and Sujit Dey. X-array: Approximating omnidirectional millimeter-wave coverage using an array of phased arrays. In *Proceedings of the 26th Annual International Conference on Mobile Computing and Networking*, pages 1–14, 2020.

[26] Renjie Zhao, Timothy Woodford, Teng Wei, Kun Qian, and Xinyu Zhang. M-cube: A millimeter-wave massive mimo software radio. In *Proceedings of the 26th Annual International Conference on Mobile Computing and Networking*, pages 1–14, 2020.

[27] R Ivan Zelaya, William Sussman, Jeremy Gummeson, Kyle Jamieson, and Wenjun Hu. Lava: fine-grained 3d indoor wireless coverage for small iot devices. In *Proceedings of the 2021 ACM SIGCOMM 2021 Conference*, pages 123–136, 2021.

[28] Qi Bi. The proximity radio access network for 5g and 6g. *IEEE Communications Magazine*, 60(1):67–73, 2022.

[29] Ertugrul Basar, Marco Di Renzo, Julien De Rosny, Merouane Debbah, Mohamed-Slim Alouini, and Rui Zhang. Wireless communications through reconfigurable intelligent surfaces. *IEEE access*, 7:116753–116773, 2019.

[30] Hou-Tong Chen, Antoinette J Taylor, and Nanfang Yu. A review of metasurfaces: physics and applications. *Reports on progress in physics*, 79(7):076401, 2016.

[31] Hui-Hsin Hsiao, Cheng Hung Chu, and Din Ping Tsai. Fundamentals and applications of metasurfaces. *Small Methods*, 1(4):1600064, 2017.

[32] Marco Di Renzo, Merouane Debbah, Dinh-Thuy Phan-Huy, Alessio Zappone, Mohamed-Slim Alouini, Chau Yuen, Vincenzo Sciancalepore, George C Alexandropoulos, Jakob Hoydis, Haris Gacanin, et al. Smart radio environments empowered by reconfigurable ai meta-surfaces:

An idea whose time has come. *EURASIP Journal on Wireless Communications and Networking*, 2019(1):1–20, 2019.

[33] Hao Pan, Lili Qiu, Bei Ouyang, Shicheng Zheng, Yongzhao Zhang, Yi-Chao Chen, and Guangtao Xue. Pmsat: Optimizing passive metasurface for low earth orbit satellite communication. In *Proceedings of the 29th Annual International Conference on Mobile Computing and Networking*, pages 1–15, 2023.

[34] Yezhou Wang, Hao Pan, Lili Qiu, Linghui Zhong, Jiting Liu, Ruichun Ma, Yi-Chao Chen, Guangtao Xue, and Ju Ren. Gpms: Enabling indoor gnss positioning using passive metasurfaces. In *Proceedings of the 30th Annual International Conference on Mobile Computing and Networking*, pages 1424–1438, 2024.

[35] Kai Guo, Qun Zheng, Zhiping Yin, and Zhongyi Guo. Generation of mode-reconfigurable and frequency-adjustable oam beams using dynamic reflective metasurface. *IEEE Access*, 8:75523–75529, 2020.

[36] Kun Woo Cho, Yasaman Ghasempour, and Kyle Jamieson. Towards dual-band reconfigurable metasurfaces for satellite networking. In *Proceedings of the 21st ACM Workshop on Hot Topics in Networks*, pages 17–23, 2022.

[37] Qingqing Wu and Rui Zhang. Towards smart and reconfigurable environment: Intelligent reflecting surface aided wireless network. *IEEE communications magazine*, 58(1):106–112, 2019.

[38] Lei Zhang, Ming Zheng Chen, Wankai Tang, Jun Yan Dai, Long Miao, Xiao Yang Zhou, Shi Jin, Qiang Cheng, and Tie Jun Cui. A wireless communication scheme based on space-and frequency-division multiplexing using digital metasurfaces. *Nature electronics*, 4(3):218–227, 2021.

[39] Lei Zhang, Xiao Qing Chen, Shuo Liu, Qian Zhang, Jie Zhao, Jun Yan Dai, Guo Dong Bai, Xiang Wan, Qiang Cheng, Giuseppe Castaldi, et al. Space-time-coding digital metasurfaces. *Nature communications*, 9(1):4334, 2018.

[40] Xinyi Li, Chao Feng, Xiaojing Wang, Yangfan Zhang, Yaxiong Xie, and Xiaojiang Chen. {RF-Bouncer}: A programmable dual-band metasurface for sub-6 wireless networks. In *20th USENIX Symposium on Networked Systems Design and Implementation (NSDI 23)*, pages 389–404, 2023.

[41] Manideep Dunna, Chi Zhang, Daniel Sievenpiper, and Dinesh Bharadia. Scattermimo: Enabling virtual mimo with smart surfaces. In *Proceedings of the 26th Annual International Conference on Mobile Computing and Networking*, pages 1–14, 2020.

[42] Artem V Boriskin, A Vorobyov, and Ronan Sauleau. Two-shell radially symmetric dielectric lenses as low-cost analogs of the luneburg lens. *IEEE transactions on antennas and propagation*, 59(8):3089–3093, 2011.

[43] Yujian Li, Lei Ge, Meie Chen, Zhan Zhang, Zheng Li, and Junhong Wang. Multibeam 3-d-printed luneburg lens fed by magnetoelectric dipole antennas for millimeter-wave mimo applications. *IEEE Transactions on Antennas and Propagation*, 67(5):2923–2933, 2019.

[44] Cong Wang, Jie Wu, and Yong-Xin Guo. A 3-d-printed multibeam dual circularly polarized luneburg lens antenna based on quasi-icosahedron models for ka-band wireless applications. *IEEE Transactions on Antennas and Propagation*, 68(8):5807–5815, 2020.

[45] Siyuan Lei, Kangkang Han, Xianlei Li, and Gao Wei. A design of broadband 3-d-printed circularly polarized spherical luneburg lens antenna for x-band. *IEEE Antennas and Wireless Propagation Letters*, 20(4):528–532, 2021.

[46] Yang Gao, Zhong-Xun Liu, Haoyu Lei, Yue-Nian Chen, Yongtao Jia, Qiao Sun, and Ying Liu. A luneburg lens-inspired flat lens antenna with high gain via reduced reflection loss. *IEEE Antennas and Wireless Propagation Letters*, 2025.

[47] Jose-Manuel Poyanco, Francisco Pizarro, and Eva Rajo-Iglesias. 3-d-printed integrated grin lens–polarizer using anisotropic materials. *IEEE Transactions on Antennas and Propagation*, 72(6):5343–5348, 2023.

[48] Ben Ikenson. Luneburg lens design enhances broadband and omnidirectional acoustic collimation and focusing. *Scilight*, 2021(49), 2021.

[49] Min Liang, Wei-Ren Ng, Kihun Chang, Kokou Gbele, Michael E. Gehm, and Hao Xin. A 3-d luneburg lens antenna fabricated by polymer jetting rapid prototyping. *IEEE Transactions on Antennas and Propagation*, 62(4):1799–1807, 2014.

[50] Justine Djounidi, Pilar Castillo-Tapia, Nelson JG Fonseca, and Oscar Quevedo-Teruel. Low-profile fully metallic multiple-ridge luneburg lens antenna. *IEEE Transactions on Antennas and Propagation*, 72(6):4852–4861, 2024.

[51] Pilar Castillo-Tapia, Shiyi Yang, Á Palomares-Caballero, J-P Guillet, NJG Fonseca, and Oscar Quevedo-Teruel. Sub-thz fully-metallic geodesic luneburg lens antenna. *IEEE Transactions on Terahertz Science and Technology*, 2025.

[52] Dan Jia, Yingran He, Ning Ding, Jianzhai Zhou, Biao Du, and Wenjing Zhang. Beam-steering flat lens antenna based on multilayer gradient index metamaterials. *IEEE Antennas and Wireless Propagation Letters*, 17(8):1510–1514, 2018.

[53] Fanyi Meng, Yue Guo, Kaixue Ma, and Yu Luo. A terahertz wide-angle beamsteering 3-d printed half-compressed elliptical luneburg lens with planar focal plane. *IEEE Antennas and Wireless Propagation Letters*, 23(2):843–847, 2023.

[54] Hao Xin, Min Liang, and Siyang Cao. Automotive radar using 3d printed luneburg lens, May 24 2022. US Patent 11,340,342.

[55] Petr Kaděra, Jesús Sánchez-Pastor, Hossein Eskandari, Tomáš Tyc, Masoud Sakaki, Martin Schüßler, Rolf Jakoby, Niels Benson, Alejandro Jiménez-Sáez, and Jaroslav Láčík. Wide-angle ceramic retroreflective luneburg lens based on quasi-conformal transformation optics for mm-wave indoor localization. *IEEE Access*, 10:41097–41111, 2022.

[56] Kun Qian, Lulu Yao, Kai Zheng, Xinyu Zhang, and Tse Nga Ng. Uniscatter: a metamaterial backscatter tag for wideband joint communication and radar sensing. In *Proceedings of the 29th Annual International Conference on Mobile Computing and Networking*, pages 1–16, 2023.

[57] Samuel Kim, Tim Sleasman, Avrami Rakovsky, Ra'id Awadallah, and David B Shrekenhamer. Dynamic metasurface-backed luneburg lens for multiplexed backscatter communication. *IEEE Access*, 2025.

[58] Haobo Zhang, Hongliang Zhang, Boya Di, Kaigui Bian, Zhu Han, Chenren Xu, Daqing Zhang, and Lingyang Song. Rss fingerprinting based multi-user outdoor localization using reconfigurable intelligent surfaces. In *2021 15th International Symposium on Medical Information and Communication Technology (ISMICT)*, pages 167–172. IEEE, 2021.

[59] Xinyi Li, Gaoteng Zhao, Ling Chen, Xinyu Zhang, and Ju Ren. Rfmagus: Programming the radio environment with networked metasurfaces. In *Proceedings of the 30th Annual International Conference on Mobile Computing and Networking*, pages 16–30, 2024.

[60] NI. Usrp-2954 specifications. Website, 2025. August 25, 2025. URL: https://www.ni.com/docs/en-US/bundle/usrp-2954-specs/page/specs.html.

[61] Lair Microwave. Rf coaxial switch spnt series. Website, 2025. August 2, 2025. URL: https://www.lairmw.com/cn/product.php?mod=detail&id=214.

[62] ANALOG DEVICES. Eval-adl6010. Website, 2025. August 2, 2025. URL: https://www.analog.com/en/resources/evaluation-hardware-and-software/evaluation-boards-kits/eval-adl6010.html#eb-overview.

[63] UIY. Rf coaxial circulator. Website, 2025. August 2, 2025. URL: https://www.uiy.com/cn/Coaxial_Circulator/.

[64] Macom. Ma4agsw8-1. Website, 2023. August 2, 2023. URL: https://www.macom.com/products/product-detail/MA4AGSW8-1.

[65] Analog Devices. Adrf5020: 4–8 ghz, 6-bit digital rf step attenuator. Website and Datasheet, 2023. Datasheet Rev. A. Accessed August 2, 2023. URL: https://www.analog.com/en/products/adrf5020.html.

[66] Changkun Technology. Bs-metabts bs5622. Website, 2025. August 29, 2025. URL: https://www.bjcktech.com/index.php/Home/Product/view/id/288.html.
[67] Changkun Technology. Ue-cp5104-oa00. Website, 2025. August 29, 2025. URL: https://www.bjcktech.com/index.php/Home/Product/view/id/262.html.
[68] NETGEAR. R6800 — ac1900 dual band gigabit wifi router. Website, 2025. August 29, 2025. URL: https://www.netgear.com/support/product/r6800/#docs.
[69] iperf tools. Magic iperf. Website, 2025. August 29, 2025. URL: https://magic-iperf-including-iperf3.soft112.com/.
[70] Cun Wang, Yulong Xia, Guangjun Guo, Muhammad Nasir, and Qi Zhu. Ellipsoidal luneburg lens binary array for wide-angle scanning. *IEEE Transactions on Antennas and Propagation*, 68(7):5702–5707, 2020.
[71] Ruolei Xu and Zhi Ning Chen. A hemispherical wide-angle beamsteering near-surface focal-plane metamaterial luneburg lens antenna using transformation-optics. *IEEE Transactions on Antennas and Propagation*, 70(6):4224–4233, 2022.

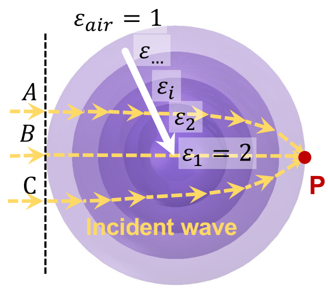

Fig. 22 – Wave propagation through a Luneburg lens.

A Geometric-Optics Model of the Lens

As shown in Figure 22, incoming electromagnetic waves pass through a series of dielectric layers whose permittivity decreases continuously from 2 at the center to 1 at the surface. This gradient-index profile ensures that wavefronts equiphase surface ABC experience progressive refraction while maintaining equal optical path length, causing them to bend and converge to a single focal point P. This model explains why a Luneburg lens inherently provides passive phase compensation and direction-dependent focusing gain. This model directly corresponds to ray-tracing analyses in Luneburg lens related reference[70, 71]. Based on this model, we can find the relationship between the physical lens parameters with beam width and gain.

Scaling of Beam Coverage and Angle Resolution with Antenna Count. The number of patch antennas N placed along the focal surface determines how finely these intrinsic beams are sampled. With more antennas, the focal positions are sampled more densely, yielding finer practical steering resolution (angular interval $\approx$ scanning range$/N$). This resolution is ultimately constrained by the minimum patch spacing, which must remain above the mutual-coupling limit ($\geq \lambda/4$). Within this bound, populating the lens surface with as many antennas as feasible enables continuous hemispherical coverage and improves steering precision. However, more antennas require more time for scanning, resulting in higher scanning latency. In OrbWeaver, with a near 180° scanning range and the available antenna count, the resulting angular resolution is 10°.

B Simulation Driven Luneburg Lens Design

To implement the controlled filling ratio distribution, we employ a cruciform cube structure whose geometry can be precisely controlled during the 3D printing process. Our design presents an engineering challenge: *How do we transform a collection of discrete cubes into a high-performance focusing system?*

Cube Structure Characterization. Each cube characterized by three main parameters: size a, pillar diameter b, and pillar height c. The parameter c should be minimized within the constraints of 3D printing resolution to enable finer dimensional control of the cubes, allowing smaller discretization steps in implementing the required permittivity gradient. The parameter b determines the cube filling ratio, which in turn affects the equivalent relative permittivity and needs to be optimized within a certain range ($c \leq b \leq a$).

The cube size a is selected to balance filling ratio flexibility and the subwavelength requirement for effective medium approximation. Specifically, when $a << \lambda$ (typically $\frac{\lambda}{10}$ to $\frac{\lambda}{4}$), the cube structure behaves as a homogeneous equivalent medium. However, this constraint conflicts with practical design needs: larger a values enable wider permittivity ranges through increased b flexibility, while smaller a values result in coarser discretization.

To resolve this trade-off, we simulated the relationship between cube size and effective permittivity extraction accuracy. As shown in Fig. 23(a), when $a = 3.2$ mm, the equivalent medium theory no longer holds, and the calculated permittivity exhibits an abnormal decrease. Conversely, a smaller a severely limits the achievable permittivity range. Therefore, we selected $a = 3mm$ as the optimal balance, the largest feasible cube size that maintains theoretical validity while providing sufficient design flexibility for the lens.

Lens Architecture Design. After determining the cube dimensions, we construct the lens structure by selecting appropriate filling ratios for each layer to achieve the required permittivity gradient. Since the lens diameter directly affects beam directivity and sidelobe levels, we evaluate lens performance using two key metrics: gain and half-power beamwidth (HPBW) across different layer configurations.

Figure 23(b) summarizes the effect of the number of dielectric layers on the lens beamforming performance. As the layer count increases, the lens exhibits improved directivity and narrower beamwidth, while the performance gain gradually saturates as the physical lens size grows. From a design standpoint, the layer count controls how closely the

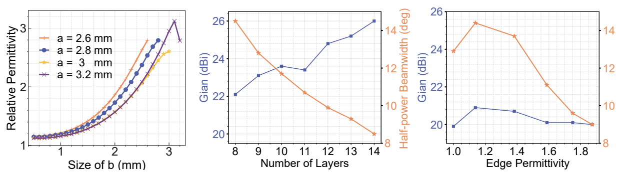

(a) cube size impact. (b) Number of layers. (c) Edge permittivity.

Fig. 23 – Impact parametric of 3D print gradient index lens design

discretized permittivity profile approximates the ideal Luneburg distribution. Increasing the number of layers reduces phase discontinuities and internal reflections, improving focusing accuracy. However, further scaling amplifies practical limitations, including fabrication tolerances, refractive-index deviations, cumulative interface reflections, and increased dielectric losses, which degrade aperture efficiency and offset the theoretical gain.

Based on this analysis, we identified 13 layers as the optimal configuration that maximizes directivity and gain while avoiding the diminishing returns and losses associated with larger lens structures.

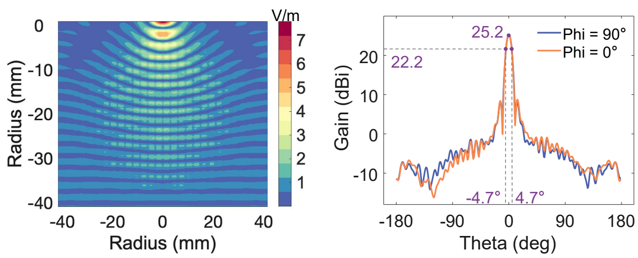

(a) Electric field (b) Far-field radiation patterns

Fig. 24 – Simulation results of the lens at 28 GHz

Performance Optimization. Having established the foundation with cubes and architecture with layers, our attention turned to critical yet often overlooked detail: the lens boundaries. The permittivity of the edge layer plays a pivotal role in impedance matching between the lens and free space, fundamentally affecting focusing performance including gain and main to sidelobe level difference. To systematically investigate this critical design parameter, we conducted comprehensive simulations that examined the relationship between edge permittivity and lens performance metrics.

We selected the edge permittivity range from 1 to 1.87, and the result in Figure 23(c) showed that while the gain of the mainlobe maintained approximately 20 dB with minor fluctuations, the main-to-sidelobe level difference varied significantly across the permittivity range. The result suggests that an edge permittivity in 1.1-1.2 provides the optimal balance, offering both maximum sidelobe suppression and stable gain performance. In our case, we select the edge permittivity of 1.1378.

Based on our systematic three-step optimization process, we finalized a 13-layer Luneburg lens design with the optimized parameters: a = 3 mm and c = 0.5 mm. The result in Figure 24(a) shows the electric field magnitude distribution across the lens cross-section, where the concentric patterns demonstrate the wave propagation and focusing behavior within the designed lens. Figure 24(b) presents the far-field radiation pattern in two planes($\varphi = 0°$ and $\varphi = 90°$) with the feed antenna mounted on the lens surface, achieving a peak gain of 22 dB and a narrow beamwidth of 4.7°